Using Vehicle-induced DAS Signals for Near-surface Characterization with High Spatiotemporal Resolution

Siyuan Yuan[1], Jingxiao Liu[1,2], Hae Young Noh[2], Robert Clapp[1], and Biondo Biondi[1]

[1]Department of Geophysics, Stanford University, Stanford, CA, USA
[2]Department of Civil and Environmental Engineering, Stanford University, Stanford, CA, USA

Key Points:

- We utilize a large number of vehicles transiting on city streets as non-dedicated seismic sources for continuous near-surface monitoring.
- Our method outperforms ambient noise interferometry in efficiency and resolution, leveraging selective cross-correlation of surface waves.
- We observed rain-induced changes in seismic properties using time-lapse analysis of kinematics and attenuation.

Corresponding author: Siyuan Yuan, syyuan@sep.stanford.edu

Abstract

Vehicle-induced seismic waves, generated as vehicles traverse the ground surface, carry valuable information for imaging the underlying near-surface structure. These waves propagate differently in the subsurface depending on soil properties at various spatial locations. By leveraging wave propagation characteristics, such as surface-wave velocity and attenuation, this study presents a novel method for near-surface monitoring. Our method employs passing vehicles as active, non-dedicated seismic sources and leverages pre-existing telecommunication fibers as large-scale and cost-effective roadside sensors empowered by Distributed Acoustic Sensing (DAS) technology. A specialized Kalman filter algorithm is integrated for automated DAS-based traffic monitoring to accurately determine vehicles' location and speed. Then, our approach uniquely leverages vehicle trajectories to isolate space-time windows containing high-quality surface waves. With known vehicle (i.e., seismic source) locations, we can effectively mitigate artifacts associated with suboptimal distribution of sources in conventional ambient noise interferometry. Compared to ambient noise interferometry, our approach enables the synthesis of virtual shot gathers with a high signal-to-noise ratio and spatiotemporal resolution at reduced computational costs. We validate the effectiveness of our method using the Stanford DAS-2 array, with a focus on capturing spatial heterogeneity and monitoring temporal variations in soil seismic properties during rainfall events. Specifically, in non-built-up areas, we observed an evident decrease in phase velocity and group velocity and an increase in attenuation due to the rainfall. Our findings illustrate our method's sensitivity and resolution in discerning variations across different spatial locations and demonstrate that our method is a promising advancement for high-resolution near-surface imaging in urban settings.

Plain Language Summary

Continuous monitoring of near-surface soil properties is important to various applications, including identifying subsidence and monitoring groundwater levels. Vehicles transiting in city streets excite seismic waves propagating in the subsurface, which can be analyzed to gain insights into the structures beneath the surface. In this study, we develop a novel near-surface monitoring method utilizing traffic recordings of Distributed Acoustic Sensing (DAS) technology, transforming existing telecommunication cables into extensive ground motion sensors. To harness the vibrations generated by vehicles, our method employs a specialized algorithm, determining vehicle locations and speeds based on the ground deformation they induce. The identified vehicle location is precisely utilized to select specific traffic-induced seismic waves to explore the subsurface. Our approach allows for the acquisition of clearer and more precise insights into underground structures in urban areas and is more computationally efficient than traditional methods based on ambient noises. Tested at Stanford University in 2023, our method adeptly identified variations in the seismic properties of the subsurface, particularly in non-built-up areas, during rainfall events. Such accurate detection is valuable for water resource management and urban development, enabling enhanced understanding and management of urban subsurface environments.

1 Introduction

In urban areas, it is useful to monitor continuously the near-surface for various purposes, including subsidence and pothole detection, as well as for improving seismic hazard analysis maps to include more site-specific effects. While traditional methods, such as controlled source surveys (Nazarian et al., 1983; Park et al., 1999; Stokoe et al., 2017), can provide high-quality near-surface images, repeatedly conducting such surveys on a large scale is challenging regarding logistics and operational expenses. To circumvent the need for expensive active source surveys, researchers have turned to ambient noise in-

terferometry (Shapiro & Campillo, 2004; Wapenaar et al., 2010) that aims to extract coherent surface-wave signals by performing cross-correlation between passive ambient noise recordings at virtual shot locations and virtual receivers at different offsets. Traditionally used with geophone arrays, this algorithm has proven effective for subsurface imaging in urban environments (Lin et al., 2013; Chang, 2018). However, deploying dense geophone arrays in urban settings on a large scale and a long-term basis presents its own set of challenges, including high operational costs and significant logistical hurdles.

Distributed Acoustic Sensing (DAS) has emerged as a promising technology in response to these challenges. DAS-based monitoring is performed by connecting an interrogator to one end of a standard telecommunications-grade optical fiber. The interrogator sends short laser pulses into the optical fiber and measures the subtle phase shifts of Rayleigh scattered light returning to the detector at a predicted two-way travel time (Posey, 2000; Masoudi & Newson, 2016). In this way, the strain field induced by natural processes (e.g., earthquakes) and urban activities (e.g., moving vehicles, construction, pumps) acting on the fiber coupled to the Earth can be sampled at a meter-scale spatial resolution over tens of linear fiber kilometers. Notably, DAS technology has proven effective on existing and growing "dark fiber" telecommunication infrastructure for earthquake monitoring (Biondi et al., 2021), infrastructure monitoring (Yuan et al., 2021; Liu, Yuan, Luo, et al., 2023), and near-surface imaging (E. R. Martin et al., 2017; Fang et al., 2020), significantly reducing installation cost. Furthermore, by incorporating state-of-the-art interrogators, such as OptaSense QuantX (Optasense, a Luna company, 2022), DAS can record full waveform signals over distances up to 50 km, with a granular 1 m channel spacing, which makes DAS promising for continuous city-wide sensing.

Just as the geophone-based techniques, DAS often harnesses ambient noise interferometry to sidestep active source surveys in subsurface characterization (E. R. Martin et al., 2017, 2021). While the conventional interferometry approach has been successful in numerous applications, it has several limitations. Firstly, it is computationally expensive because it requires cross-correlation of days or even weeks of noisy recordings to reach convergence, depending on the relative strength of signals and noise. This computational burden intensifies when using DAS, given its abundance of channels. The lengthy cross-correlation period also results in diminished temporal resolution, which may not capture sudden subsurface changes caused by floods or construction. Secondly, passive interferometry relies on the assumption that the incident azimuth of the wave field generated by the sources is uniformly distributed, which may not hold in practice. The noise sources may be localized, heterogeneous, and time-dependent, leading to inaccurate results. Thirdly, capturing high-quality, high-frequency signals (above 10 Hz) using ambient noise interferometry presents a challenge due to the dominance of lower-frequency vibrations in ambient noise. While passing vehicles can generate strong high-frequency energy, this energy attenuates more rapidly as it propagates than lower frequencies. As a result, the high frequencies often remain undetected when cross-correlating without specific targeting. Therefore, the method may miss important subsurface information in the high-frequency range that is relevant for detecting small-scale and shallow features, such as fractures or cracks.

To overcome the aforementioned challenges associated with ambient noise interferometry, we propose a novel approach that utilizes regular, everyday vehicles as active and non-dedicated seismic sources in a roadside DAS array. Specifically, our approach capitalizes on a prevalent urban dark fiber setup in which the DAS array is aligned parallel to the roadway. This configuration enables the DAS to effectively record the seismic signals of vehicles as they transit along the road. The trajectories of the vehicles can be automatically detected and tracked by the Kalman filter algorithm that we designed for a DAS-based traffic monitoring system (Liu, Yuan, Dong, et al., 2023). Leveraging these accurately identified trajectories, we can efficiently isolate high-quality, vehicle-induced surface waves for advanced subsurface characterization.

The unique advantage of our method is its ability to leverage the knowledge of vehicle trajectories, from which we select space-time windows containing high-quality surface waves from isolated vehicles. Unlike ambient noise interferometry, which requires cross-correlation of days or weeks of recordings from unknown ambient noise sources, we streamline the process and only cross-correlate the data in these selected windows with the benefits of known source locations. Our approach enables us to construct high signal-to-noise ratio virtual shot gathers efficiently, reducing computational costs significantly. By stacking the results of hundreds of automatically tracked vehicles, we can obtain a highly accurate virtual shot gather containing subsurface information with a temporal resolution of one day, which is difficult to achieve with conventional interferometry. Furthermore, our method eliminates issues arising from uneven distribution of wave azimuth angles, thanks to our knowledge of the source locations. Finally, by utilizing the precise locations of the transiting vehicles, we are able to target and capture rapidly attenuated high-frequencies excited by the vehicles, enabling effective imaging of shallow subsurface structures.

Our method represents a generalized solution capable of providing high spatial-temporal resolution for urban near-surface imaging. We demonstrate its efficacy via studies conducted using the Stanford DAS-2 array. Our primary aim is to capture spatial heterogeneity and track temporal modifications in near-surface seismic properties — specifically, phase and group velocity, and seismic attenuation — observed during the 2023 San Francisco Bay Area rainfall events. Alterations in these seismic properties can serve as indicators to estimate soil saturation levels with the application of rock physics principles and assumptions. The results from the analyses highlight our method's robust capability to accurately detect spatiotemporal variations in soil properties, thereby offering an enhanced approach to urban subsurface characterization.

2 Existing work on continuous subsurface characterization with DAS

Surface waves, originating from traffic or other natural or anthropogenic sources, can provide valuable insights into subsurface soil characteristics. Traditional interferometric methods allow the extraction of phase and group velocities of these waves, which can then be inverted to reveal depth-dependent subsurface elastic parameters (Dou et al., 2017; E. Martin et al., 2017). Several researchers have used the combination of DAS and interferometry for continuous subsurface monitoring. Notably, Shen (2022) applied DAS in a suburban setting, leveraging ambient noise data to explore subsurface water content changes over a two-year span. Yang and Shragge (2023) deployed an urban DAS array in Perth, Australia, and applied ambient seismic interferometry to detect subsurface variations over a ten-month period. They recorded up to 9.4% seasonal variations in depth-averaged S-wave velocity estimates, inversely correlated with local rainfall patterns, indicating changes in near-surface groundwater content. Despite these successes, conventional "blind" interferometry can be computationally intensive and potentially skewed due to the less-than-ideal positioning of seismic sources, such as vehicles, relative to the sensors. In response, Yuan et al. (2020) proposed a cost-effective approach that capitalizes more efficiently on vehicle signals. By manually isolating signals from 33 distinct vehicles passing a section of the Stanford DAS-2 array and utilizing the directly excited surface waves, they were able to invert a shear wave velocity (V_S) profile that corresponded with an independent geotechnical survey, using only vehicle-induced signals. Importantly, Yuan et al. (2020)'s approach delivers high-temporal resolution characterization as it achieves imaging from vehicle signals within a 2-hour window, significantly shorter than the days or weeks typically required for ambient noise interferometry. In addition, the known location of the sources (vehicles) bypasses the challenge presented in ambient noise interferometry of not having waves from sources spanning all azimuths. This innovative strategy represents a notable advancement in efficient and accurate urban subsurface characterization. Our research extends the work of Yuan et al. (2020). The primary advance-

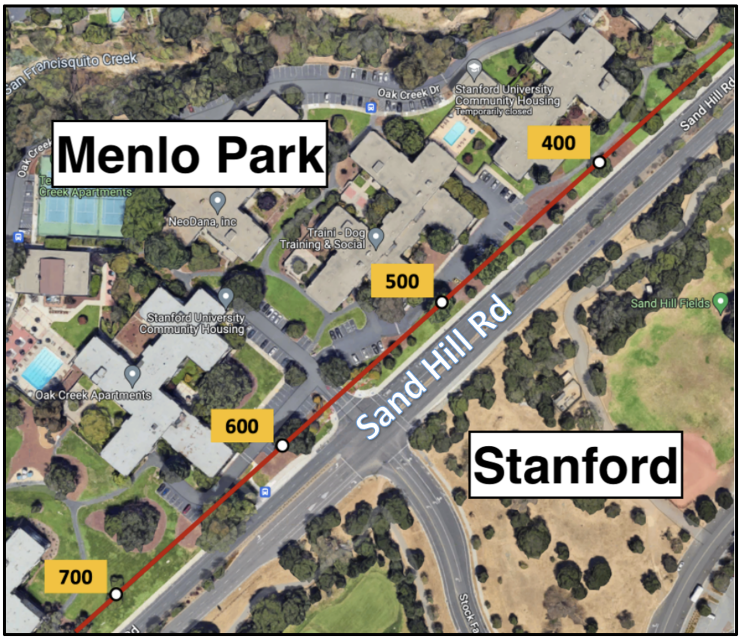

Figure 1. Map view of a roadside section of the Stanford DAS-2 Array. Distances along the fiber are labeled on the map.

ment we introduce is the automation of the previously manual and time-intensive vehicle selection process. This enhancement allows for the incorporation of hundreds of vehicles each day, markedly improving the reliability of subsurface monitoring.

3 Experimental setup

The Stanford DAS-2 experiment carried out at Stanford University has been continuously recording data since December 10, 2019. Utilizing an OptaSense ODH-3 interrogator, the experiment operates at a sampling rate of 250 samples per second, with a gauge length of 16 m. The array consists of 1250 channels in total, each spaced 8.16 m apart. Figure 1 illustrates a section of the fiber along Sand Hill Road. This section was specifically chosen due to its complex and varied nature, which represents realistic urban sensing scenarios. The fiber traverses locations with differing soil properties, such as pavement and grass. This variation presents a comprehensive and challenging test bed for our methodologies. The winter of 2023, characterized by recurrent atmospheric rivers leading to heavy rainfall, posed an unusual weather pattern in the San Francisco Bay Area. This scenario provided an excellent opportunity to evaluate both the spatial resolution and the effectiveness of our method in detecting and analyzing changes in soil saturation levels due to these rain events.

4 Proposed precision interferometry method for selective surface wave capture

The study introduces a precision interferometry method designed for the automated capture of traffic-induced surface waves and the synthesis of virtual shot gathers, facilitating continuous near-surface monitoring. We leverage a Kalman-filter-based vehicle tracking algorithm (Liu, Yuan, Dong, et al., 2023) to automatically select high-quality surface-wave windows, enhancing the methodology developed by Yuan et al. (2020). To improve the dispersion image quality and utilize signals from multiple vehicles, we con-

struct virtual shot gathers leveraging the trajectory information of each passing vehicle and then stacking the amplitudes of the virtual shot gathers for hundreds of vehicles to increase the signal-to-noise ratio (SNR). Time-lapse analyses are conducted based on the virtual shot gather in a rainfall monitoring case study.

4.1 Proposed workflow

Our proposed workflow, illustrated in Figure 2, encompasses a series of steps designed to segregate and process traffic recordings, detect and track vehicle movements, select time-space windows of surface waves, and finally, construct efficient virtual shot gathers for advanced multi-channel analyses. The workflow starts with the separation of full-bandwidth traffic recordings into quasi-static and surface wave components through bandpass filtering. We then apply a Kalman filter algorithm to the quasi-static signals to detect and track vehicles. Leveraging the output vehicle trajectories, we select time-space windows of the surface waves generated by isolated vehicles. By cross-correlating only the selected windows, we can efficiently construct virtual shot gathers that enable multi-channel analyses for time-lapse near-surface characterization.

4.2 Automatic surface-wave window selection based on vehicle-tracking

The Kalman filter algorithm (Liu, Yuan, Dong, et al., 2023), applied to quasi-static signals of moving vehicles, generates the trajectories of all detected vehicles. Figure 3 illustrates the selection process for surface-wave windows based on these tracking results. We've centered the tracking and selected surface wave windows around a pivot trace of 650 m in this example.

To prevent cross-talk among closely traveling vehicles, we select isolated vehicles by applying a time threshold parameter, denoted as $\Delta\tau$. Specifically, vehicles that reach the pivot trace within time differences smaller than $\Delta\tau$ are considered too proximate and are therefore excluded. The yellow boxes in Figure 3 represent the surface-wave windows of these isolated vehicles, selected with a $\Delta\tau$ value of 25 s.

A closer look at the surface waves from one of the selected yellow boxes is provided in Figure 4 (b). The zoomed-in view reveals the presence of two types of waves - forward and backward-propagating waves. The forward waves refer to the waves propagating in the same direction as the vehicle's movement. Conversely, the backward waves are seen propagating in the opposite direction to the vehicle's movement.

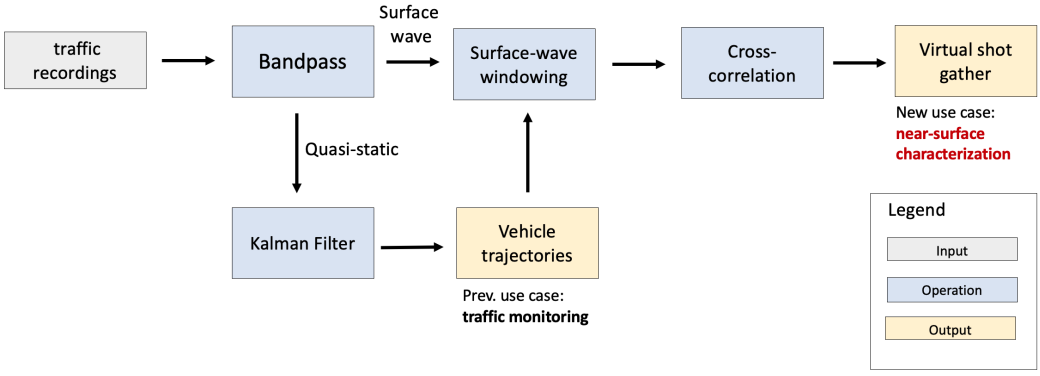

Figure 2. Workflow of the proposed vehicle-tracking imaging method.

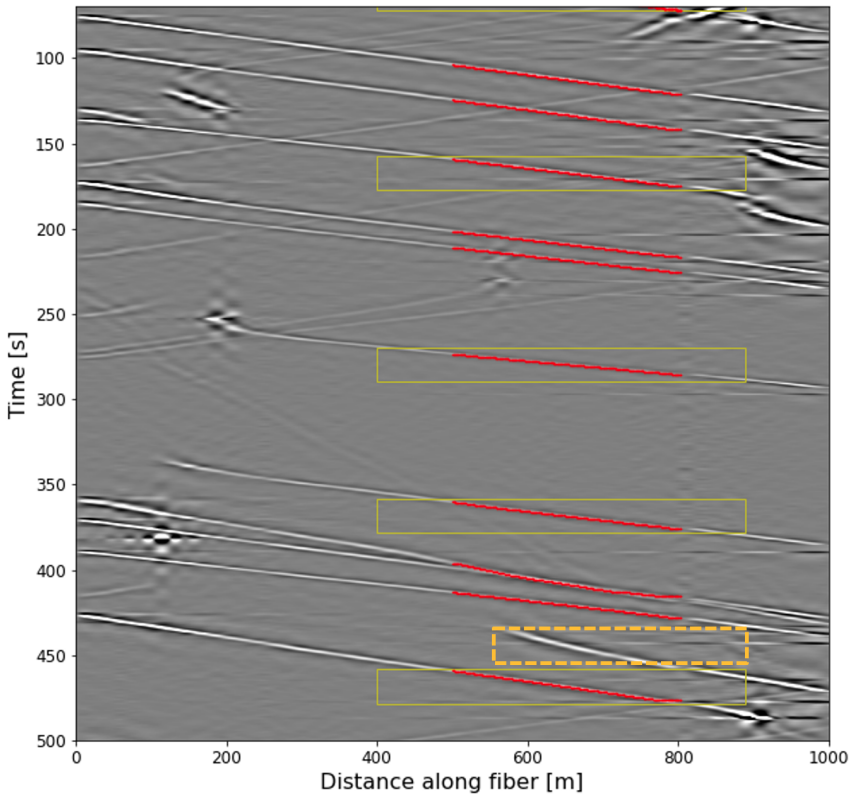

Figure 3. An example of the selection of time-space windows of the vehicle-induced surface wave for a virtual shot location, $x_0 = 650$. Vehicle trajectories from the Kalman filter algorithm are indicated in red. Yellow boxes centered at x_0 indicate isolated vehicles. The dashed orange box points to a vehicle that remains undetected because it enters Sand Hill Road from an intersection beyond the starting point of detection and tracking by the Kalman filter.

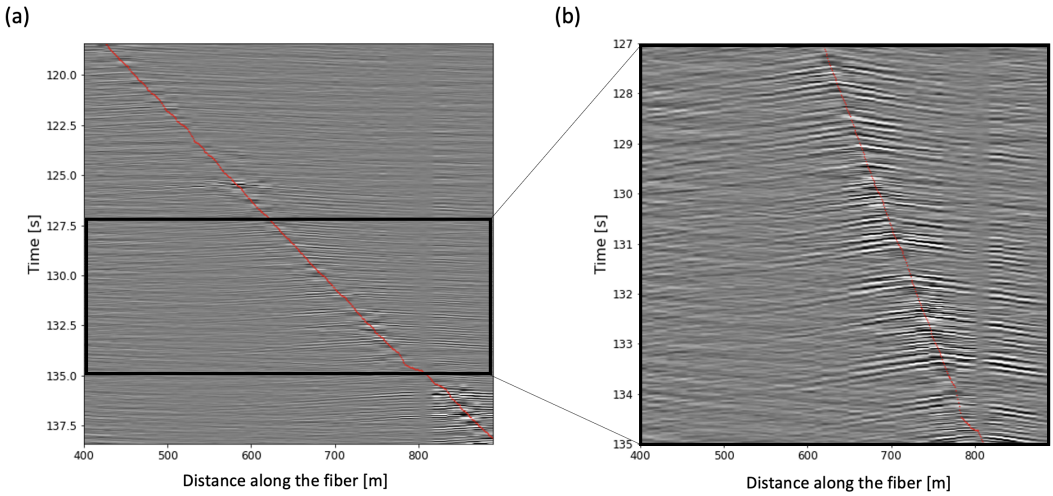

Figure 4. (a) Surface-wave component of one of the selected isolated vehicles. (b) A zoomed-in view of the surface wave.

4.3 Virtual shot gather synthesis

Utilizing surface waves, we construct virtual shot gathers via cross-correlation of the pivot trace with other traces. This process is informed by the identified vehicle trajectories. A simplified illustration of surface waves generated by a vehicle is presented in Figure 5, with forward-propagating waves denoted in yellow and backward-propagating waves denoted in orange. Two snapshots, Figures 5 (a) and (b), depict the vehicle to the left and right of the virtual shot, respectively. The color-filled receivers represent those that are located on the same side as the virtual shot relative to the vehicle, with their color matching the wavefield. By cross-correlating the recorded data at the virtual shot location with the data collected by the color-matched receivers, virtual shot gathers are constructed. Receivers represented by empty circles are not used for cross-correlation, as they are not within the same wavefield as the virtual shot.

To elaborate further, we start by defining a virtual shot at location x_s. Using the identified vehicle trajectory, we pinpoint the vehicle's arrival time at x_s, denoted as t_s. We then construct the virtual shot gathers utilizing both the forward and backward-propagating waves. Here, we first explain the assembly process of the virtual shot gather using backward-propagating waves, which propagate in the opposite direction to the vehicle's movement.

The formation of the negative offset section of the virtual shot gather is achieved by cross-correlating the recordings of the trace at virtual shot location with the receivers situated to the left of x_s ($x_r < x_s$). As can be seen in Figure 5, the virtual shot at x_s encounters forward-propagating waves before the vehicle crosses x_s, i.e., when $t < t_s$. After the point $t \geq t_s$, the vehicle has already traversed past x_s, and both the virtual shot and the receivers to the left of x_s are exposed to the same backward-propagating wavefields. Therefore, to implement the cross-correlation, we establish a time window of length Δt, within the interval $(t_s+\epsilon, t_s+\epsilon+\Delta t)$. We introduce the additional term ϵ to reduce the influence of near-field effects. This operation results in the negative-offset portion of the virtual shot gather, which can be represented by the following equation:

$$C(\tau, x_r - x_s) = \int_{t_s+\epsilon}^{t_s+\epsilon+\Delta t} d(t+\tau, x_r) \cdot d(t, x_s) dt, \tag{1}$$

where $d(t, x_s)$ is the strain at the virtual shot location x_s, $d(t, x_r)$ is the strain at a virtual receiver location x_r situated to the left of x_s ($x_s > x_r$), and τ is the time lag.

Creating the positive-offset section from the backward propagating waves requires cross-correlation of the receivers located to the right of the virtual shot ($x_r > x_s$). This process demands a different time window, expressed as $(t_r + \epsilon, t_r + \epsilon + \Delta t)$. Here, t_r represents the vehicle's arrival time at a specific receiver location x_r, as informed by the identified trajectory. This change is crucial because these receivers only experience the backward-propagating wavefield once the vehicle, traversing its path, crosses x_s and reaches the virtual receiver position, as visualized in Figure 5 (b). Additionally, since the waves move from x_r to x_s, the time offset, τ, is negated during cross-correlation to generate causal virtual shot gathers. The modified equation for cross-correlation in the positive-offset section consequently becomes:

$$C(\tau, x_r - x_s) = \int_{t_r+\epsilon}^{t_r+\epsilon+\Delta t} d(t-\tau, x_r) \cdot d(t, x_s) dt. \tag{2}$$

Equations 1 and 2 together provide the complete virtual shot gather, including both the negative and positive offset sections, which are constructed utilizing the backward propagating wavefields.

In dealing with forward-propagating wavefields, our method reconfigures the cross-correlation time windows. For synthesizing the negative-offset segment ($x_r < x_s$), we

opt for the time interval of $(t_r - \epsilon - \Delta t, t_r - \epsilon)$, where t_r denotes the vehicle's arrival times at x_r as determined by the Kalman filter trajectory. We select this time window because, within it, the vehicle hasn't yet reached x_r, and both x_s and x_r are subjected to the forward propagating wavefield. For the assembly of the positive-offset portion, we involve the receivers situated to the right of x_s. They intersect with the forward-propagating wavefields until the vehicle passes x_s. We select the time window $(t_s - \epsilon - \Delta t, t_s - \epsilon)$ for cross-correlation, resulting in the positive-offset section of the virtual shot gather.

As a concrete example, Figure 6 panels (a) and (b) show the virtual shot gathers obtained from the forward-propagating and backward-propagating wavefields depicted in Figure 4, respectively. Figure 6 panel (c) displays the virtual shot gather obtained by combining panels (a) and (b). In this combined gather, the signals are amplified due to the process of constructive interference, where signals of the gathers from the forward and backward-propagating wavefields augment each other, leading to an increase in the overall signal strength. This amplification enhances the SNR of the combined virtual shot gathers.

4.4 Improving signal-to-noise ratio (SNR) through stacking virtual shot gathers

To enhance the quality of the constructed virtual shot gathers, our methodology employs daily detection and examination of between 150 to 250 unique vehicles. By leveraging the average of their individual virtual shot gathers, we increase the Signal-to-Noise

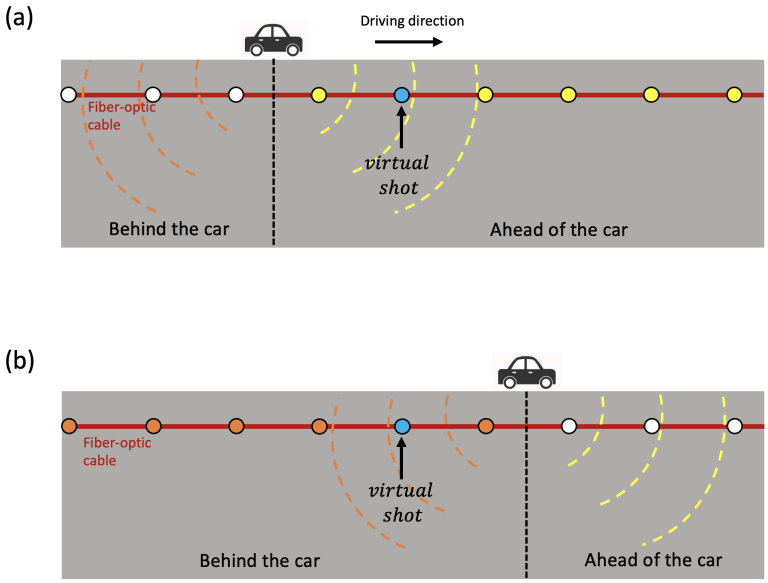

Figure 5. The diagram presents a simplified illustration of surface waves generated by a vehicle, with forward-propagating waves shown in yellow and backward-propagating waves shown in orange. Two snapshots are shown in panels (a) and (b), depicting the car to the left and right of the virtual shot, respectively. Color-filled receivers are located on the same side of the vehicle as the receiver at the virtual shot location. As such, they are subject to the same forward or backward propagating waves. To illustrate this, they are colored to match the respective waves. Virtual shot gathers can be constructed by cross-correlating the recorded data at the virtual shot location with the data collected by the color-matched receivers.

Ratio (SNR) due to the signal's constructive averaging and the noise's cancellation effects. Notably, the number of vehicles examined can vary depending on the required SNR and the time scale of the subsurface variation of interest. For a higher SNR or a longer time scale of interest, a larger number of vehicles can be utilized. Conversely, for capturing changes in soil properties at a finer temporal resolution, a smaller number of vehicles within a shorter time frame should be utilized.

The impact of this multi-vehicle virtual shot gather stacking approach can be seen in Figure 7. It showcases averages of virtual shot gathers related to varying numbers of passing cars at the same fiber location: 4 cars (panel a), 41 cars (panel b), and 173 cars (panel c). The corresponding dispersion images derived from negative-offset signals are also displayed in panels (d), (e), and (f), respectively. The displayed dispersion images are normalized at each frequency by the L-1 norm. This method of normalization is uniformly applied to the dispersion images in all the figures throughout this paper. We can see that with a stack of only 4 cars, both the virtual shot gather and the dispersion image are significantly noisy. However, when the stack includes hundreds of vehicles, the quality visibly improves. Particularly, higher modes can be discerned more clearly.

In the ideal scenario, virtual shot gathers should be purely causal. However, upon examining Figures 7, one can notice faint yet coherent signals in the negative τ region. This unexpected energy emanates from various sources: waves produced by undetected vehicles, such as the one highlighted in the dashed box of Figure 3; vehicles traveling in the distant opposing traffic lanes which were not explicitly used in our analysis due to their low amplitude and the challenges in accurately tracking them; waves resulting from other ambient noise sources with different kinematic patterns.

4.5 Comparisons with ambient noise interferometry: better resolution and less computational expense

Figure 8 offers a comparative analysis of our innovative method and the traditional ambient noise interferometry approach. Panels (a) and (c) respectively display the virtual shot gathers constructed from the same absolute eight-hour time window for DAS recording using ambient noise interferometry and our method. Panels (b) and (d) present the corresponding dispersion images.

From the virtual shot gathers, it is clear that while both methods yield waveforms with consistent moveouts, our approach recovers a significantly greater amount of high-frequency energy. The dispersion images further demonstrate that both the fundamen-

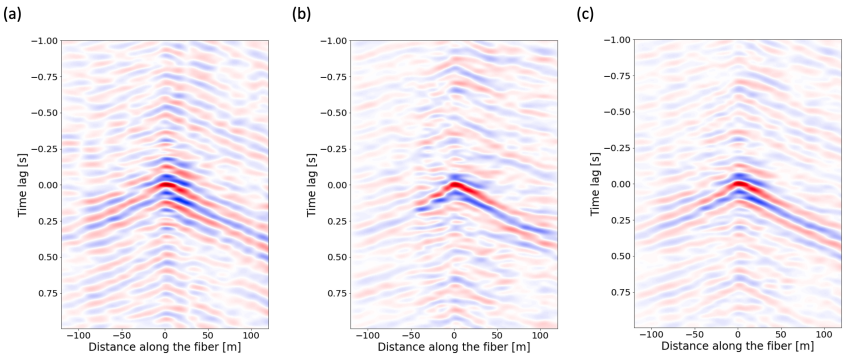

Figure 6. Panels (a) and (b) show the virtual shot gathers obtained using the forward-propagating and backward-propagating wavefields shown in Figure 4, respectively. Panel (c) is the virtual shot gather obtained by combining panels (a) and (b).

tal and overtone modes from our results are more sharply defined compared to those from the ambient noise interferometry approach. It's noteworthy that ambient noise interferometry does maintain superior signal quality below 5 Hz, which is advantageous for imaging deeper earth structures. In terms of computational costs, our method processed 200 isolated vehicles detected over the eight-hour period. For each vehicle, we cross-correlated recording in a 20-second time window, amounting to roughly 1.1 hours of data processing. In contrast, ambient noise interferometry required cross-correlation of the entire eight-hour recording. These comparisons underscore the enhanced effectiveness and efficiency of our novel approach, highlighting its potential to deliver superior results while reducing computational demands.

5 Investigation of near-surface spatial heterogeneity

Leveraging the virtual shot gathers assembled along the fiber, we conduct an in-depth spatial characterization of the near surface. This involves both kinematic and amplitude analyses. The kinematic analysis focuses on the phase- and group velocity, while the amplitude analysis is centered on the assessment of seismic attenuation.

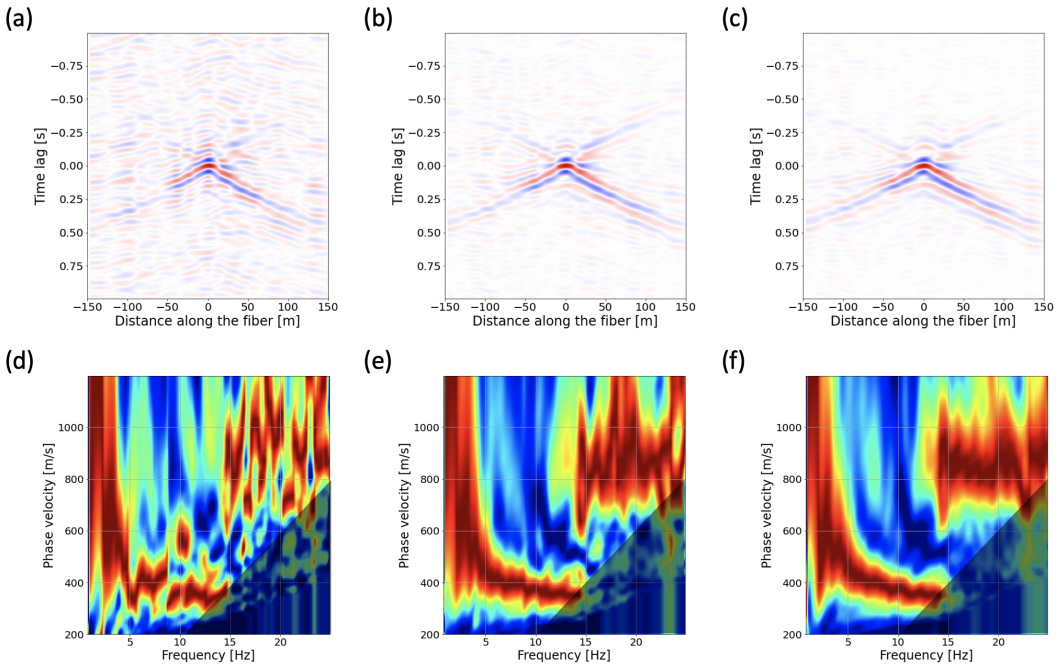

Figure 7. Panels (a), (b), and (c) show the average of virtual shot gathers for 4, 41, and 173 passing cars, respectively, at a fixed fiber location. Panels (d), (e), and (f) show their corresponding dispersion images using the negative-offset signals. Each frequency in these images is normalized by the L-1 norm. This normalization method is consistently applied throughout all dispersion images in this paper. Shaded areas show spatial high-cut filters caused by finite gauge length (16 m).

5.1 Kinematic characterization: dispersion analyses and group velocity tomography

5.1.1 Spatial heterogeneity uncovered through dispersion analysis

For dispersion analysis, we use the frequency-wavenumber method (Louie, 2001) to compute dispersion images from the virtual shot gathers to obtain phase velocities for different frequencies. Figure 9 provides a series of maps and images. Panel (a) offers a zoomed-in view of a map for a non-built-up area, with the virtual shot location indicated by a red arrow. Panel (b) shows the virtual shot gather for this area, and panel (c) presents the corresponding dispersion image derived from the negative-offset signals. In contrast, panel (d) provides a zoomed-in view of a built-up area's map, where the virtual shot location is also marked by a red arrow. Panel (e) presents the virtual shot gather for this built-up area, and panel (f) shows the corresponding dispersion image using the negative-offset signals.

Comparing the virtual shot gathers from these two locations, we observe faster wave propagation in the built-up region due to the greater compactness of the soil beneath the fiber in this constructed zone. The dispersion images confirm this increased speed in the built-up area. Notably, in panel (f), a bifurcation is evident between 10 and 15 Hz due to lateral heterogeneity. We note energy around 350 m/s, consistent with the ve-

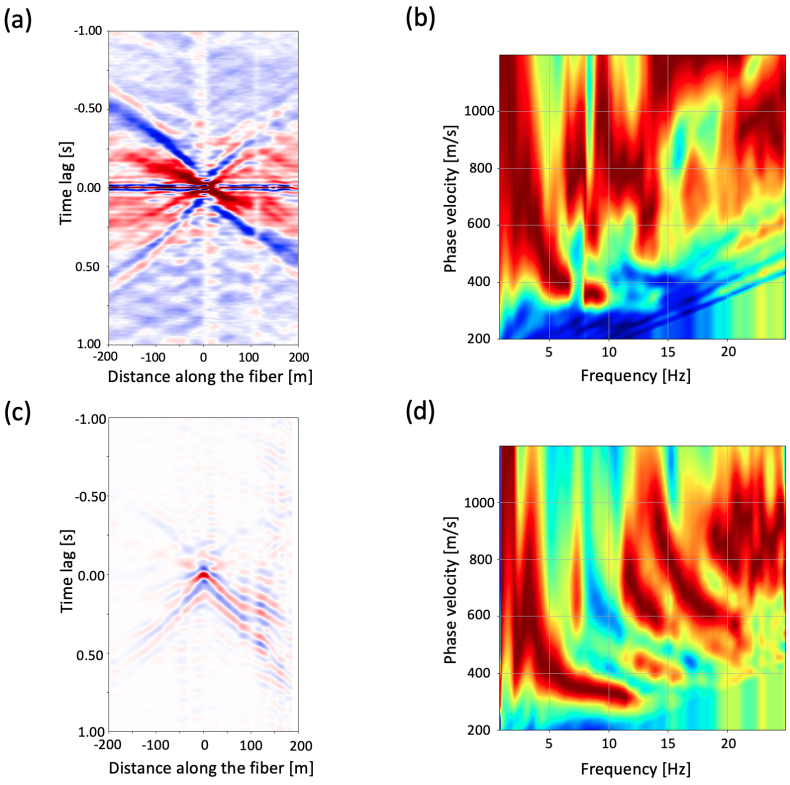

Figure 8. Comparisons between ambient noise interferometry and our method using the same eight-hour time window of DAS recording. Panels (a) and (b) are, respectively, the virtual shot gather and the corresponding dispersion image obtained using the ambient noise interferometry approach. Panels (c) and (d) are the results obtained using our vehicle-tracking-based imaging approach. Both the fundamental and overtones are resolved much better than interferometry.

locity in the non-built-up location, and a faster velocity of about 400 m/s, which could relate to the compacted soil at the building foundation in the built-up area.

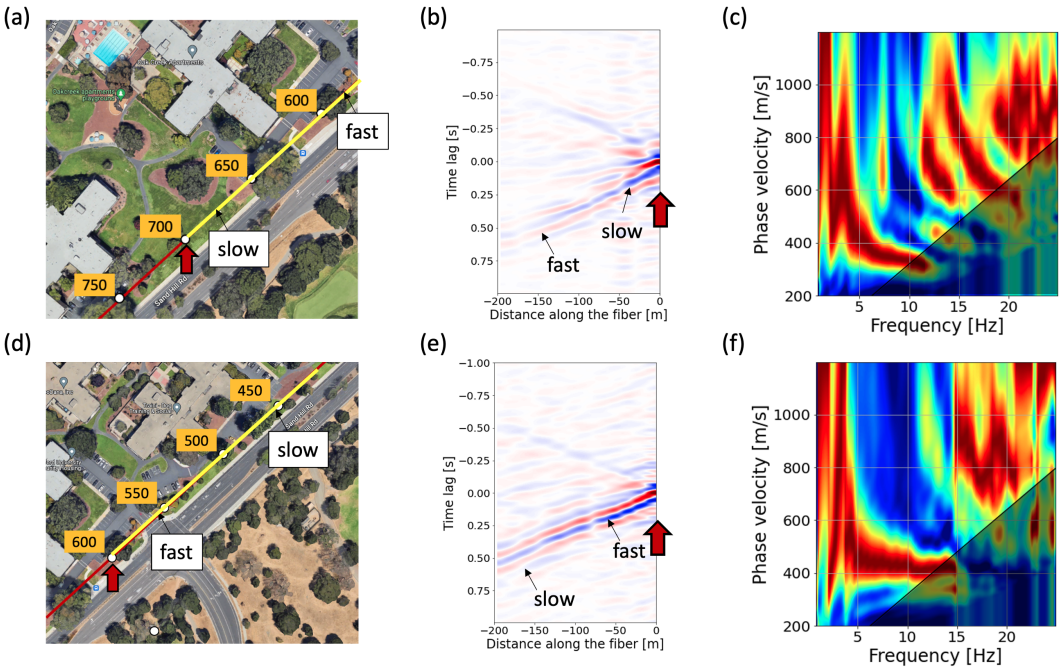

Figure 9. (a) Zoomed-in view of the map of a non-built-up region. (b) is the virtual shot gather (virtual shot location is indicated with a red arrow in (a)). (c) is the dispersion image using the negative-offset signals. (d) shows a zoomed-in view of the map of a built-up region. (e) and (f) are the virtual shot gather (virtual shot location is indicated with a red arrow in (d)) and the dispersion image using the negative-offset signals. Bifurcation due to lateral heterogeneity can be observed between 10 and 15 Hz.

Phase-velocity dispersion analyses operate under the assumption of consistent lateral velocities. Yet, as Figure 9 (f) illustrates, such uniformity isn't always present along Sand Hill Road. The bifurcation can introduce errors in selecting the appropriate phase velocity. To offer a solution to this challenge, the next subsection explores group velocity tomography, aiming for a detailed estimation of group velocities along the fiber.

5.1.2 Group-velocity tomography

To capture spatial heterogeneity in imaging, the straight-ray tomography method is presented by Shapiro et al. (2005); Lin et al. (2008); de Ridder and Dellinger (2011) to generate high-resolution group velocity maps through arrival time measurements. We adapt this concept to implement a method of 1-D group-velocity tomography that can be performed in two steps: travel-time picking and interal velocity least-square fitting. To perform travel-time picking, we use a continuous wavelet transform (CWT) approach on multiple virtual shot gathers with sources at different locations to extract the travel times of a dominant frequency. Next, we compute the local time derivative at each fiber location to obtain a rough estimate of the group velocity. To obtain smoother estimates, we employ an interval velocity inversion approach. We do this by matching the predicted group velocity through a least squares approach and using a smoothing operator that penalizes the second derivative of the predicted group velocity. This can be formulated mathematically as minimizing:

$$||m - v||_2^2 + \lambda||\nabla^2 m||_2^2, \tag{3}$$

where m represents the interval velocity model to estimate, and v represents the measured group velocity obtained from travel-time picking. The second term on the right-hand side is a regularization term that penalizes the roughness of the estimated model. The parameter λ controls the trade-off between data fidelity and model smoothness.

To improve the accuracy and reliability of the travel-time estimates, we average virtual shot gathers from approximately 2800 vehicles over a two-week period for each fiber segment. The group-velocity profile for each segment is then determined by solving the least-squares fitting problem with the loss function in Equation 3. For each spatial location, we take the median of the estimated group velocity from all the virtual shot gathers that cover it. The group-velocity profiles for 6, 7, and 8 Hz along the fiber are depicted in Figure 10. According to (Aki & Richards, 2002), group-velocity images possess a depth-integrated sensitivity, peaking at approximately half the wavelength. For the frequencies analyzed, the respective depth sensitivities are 30 m, 25 m, and 21 m.

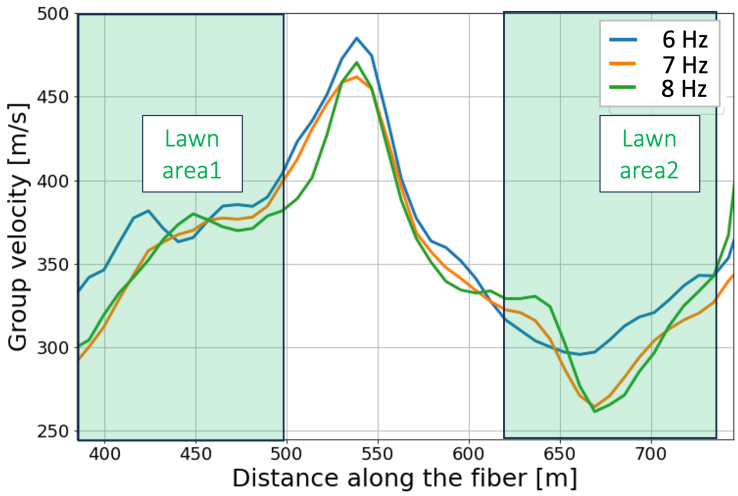

Figure 10. Estimated group velocity profile along the fiber line for 6, 7, and 8 Hz. Depth sensitivities for these frequencies are approximately 30 m, 25 m, and 21 m, respectively.

By comparing these profiles with the map in Figure 1, a strong correlation can be observed between the profile and the geotechnical conditions along the fiber. Particularly, an increase in group velocity from 380 m to roughly 540 m is evident, corresponding to the DAS fiber passing through areas from the lawn to the built-up zone. This transition is marked by a paved parking lot around the 540-meter mark, as shown on the map. Beyond this point, the group velocity begins to decline from approximately 540 m to 650 m as the fiber traverses from the constructed zone to a second lawn region. This observation aligns with our understanding that higher group velocities suggest a more compact subsurface. Additionally, in lawn regions, the 6 Hz profile, which is more sensitive to deeper depths, typically exhibits a higher group velocity—evident between 650 m and 720 m. This suggests a more stratified subsurface. Conversely, in the built-up area, especially from 500 m to 600 m, the velocity profiles for all three frequencies are comparable. This similarity suggests a more uniform subsurface due to the homogenization and compaction from construction activities.

5.2 Amplitude Analysis: seismic attenuation

Our methodology utilizes the spectral ratio method to investigate the spatial heterogeneity of the seismic attenuation level along the fiber, denoted as Q^{-1}. Our approach aligns with the technique used by (Zhao et al., 2023). to extract seismic attenuation from traffic signals using a single seismic station. However, we enhance the reliability of our Q^{-1} estimates by incorporating DAS technology, which allows us to leverage multi-channel recordings. The first step of our method involves converting the virtual shot gather to the frequency-distance domain via a Fourier Transform for each trace. According to the equation 4, the logarithm of the spectral ratio between two traces is linearly related to the distance separating these traces, with Q^{-1} being proportional to the slope.

$$ln\left(\frac{A_1}{A_2}\right) = C - \frac{\pi(x_2 - x_1)}{Qv} f, \tag{4}$$

where A_1 and A_2 represent the amplitudes of the spectrum for frequency f for traces 1 and 2, respectively. The constant C is the intercept term of the linear relationship. v stands for surface-wave velocity. We select the trace at x_0 of a virtual shot gather as the reference trace and compute the spectral ratio of this reference trace to the traces at distance x. A linear line representing the logarithm of the spectral ratio versus x is fitted via a least squares method to estimate Q^{-1} for some dominant frequencies.

Figure 11 illustrates the Q^{-1} estimation process using a fiber subsection as an example. Panel (a) depicts the negative-offset virtual shot gather with the virtual shot's position at 580 m. In panel (b), the variation in spectral amplitude with distance offset is presented, derived from a trace-wise Fourier transform. It's evident that higher frequencies attenuate more rapidly than lower ones, aligning with our expectations. Moreover, the majority of the energy is concentrated within the initial 50 m. Consequently, our Q^{-1} estimation focuses on this first 50 m, as shown in panel (c). This panel depicts the logarithmic spectral ratio between each virtual receiver and the virtual shot recording with dots, suggesting a linear relationship. Employing a least-squares fitting method, we obtain the solid lines for frequencies 8 and 10 Hz. With the slopes of these lines and surface-wave velocity extracted from the dispersion curve estimated in this fiber subsection, we estimated the Q^{-1} factors to be 0.5 and 0.45 for 8 and 10 Hz, respectively.

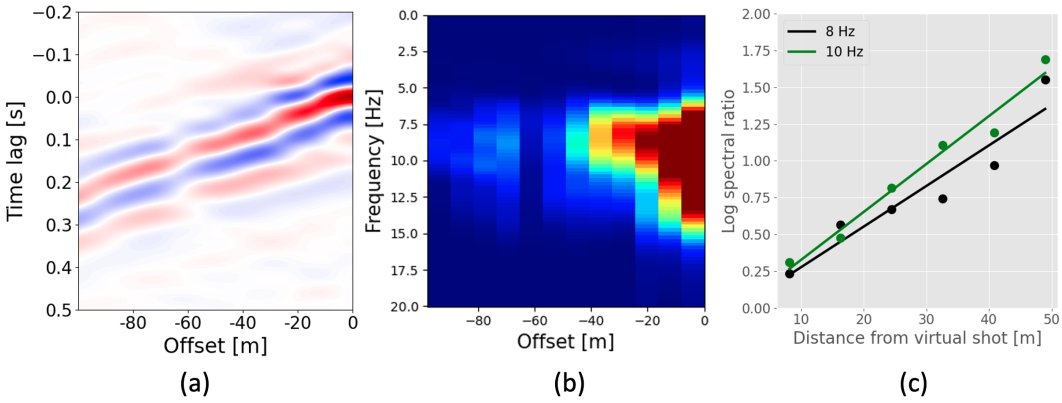

Figure 11. Illustration of the Q^{-1} estimation process over a location range spanned by a fiber subsection. (a) Negative-offset virtual shot gather, with the virtual shot located at 580 m; (b) Spectral variation as a function of distance offset; (c) Dots depict the log spectral ratio of each virtual receiver relative to the virtual shot recording. The solid lines represent the least-square fitted trends, and their slopes are used to compute the Q^{-1} value.

We performed an analysis using the virtual shot gathers generated along the fiber to study the Q^{-1} profile. To ensure reliable estimates, we averaged the virtual shot gathers from approximately 2800 vehicles detected over a two-week span for each fiber segment. The Q^{-1} value derived from these recordings is assigned to the midpoint of each fiber segment. Figure 12 displays the derived Q^{-1} profile based on recordings from two consecutive dry weeks. Comparing this profile with the group velocity depicted in Figure 10, it is clear that constructed areas with a higher group velocity tend to have lower attenuation. In contrast, the two lawns show higher seismic attenuation than the paved area.

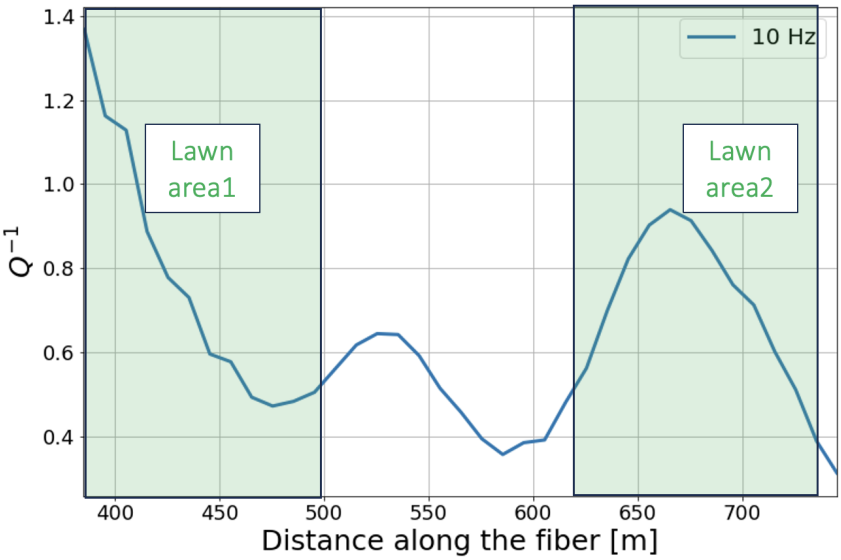

Figure 12. Profile of Q^{-1} attenuation values along the fiber-optic cable. Elevated levels of seismic attenuation are observed in the non-constructed lawn areas, which are possibly linked to the high clay content in the subsurface soil.

6 Time-lapse analysis of soil property variations

In this section, we conduct both kinematic and amplitude analyses of virtual shot gathers constructed over a seven-month duration. This time-lapse study highlights the efficacy of our proposed method in tracking alterations in soil saturation caused by rainfall events.

6.1 Phase velocity variation and rainfall correlation

We first investigate the influence of varying rainfall volumes on the phase velocity changes within two distinct sections of fiber optic cables from early December 2022 until the middle of July 2023. The first cable section, found underneath a paved road, extends from 490 m to 590 m. The second section, nested beneath a grassy terrain, spans from 610 m to 710 m. Figure 13 (a) and (b) showcase the phase velocities, specifically at frequencies of 6, 8, and 10 Hz, selected from the dispersion images of the daily constructed virtual shot gathers, corresponding to the paved and grassy regions, respectively.

An observable decline in phase velocity is evident in the grassy area corresponding to Figure 13 (b) following substantial rainfall from the end of December to early January. During the comparatively drier period towards the end of January, there's a slight

resurgence in phase velocity. However, this increase is short-lived as the phase velocity dips again with the onset of rain during February and March's wet conditions. From April to July, characterized as drier months, a gradual recovery in phase velocity can be noted. Comparatively, in the built-up area corresponding to Figure 13 (a), the impact of rainfall events on the phase velocity's temporal variation is not as pronounced, indicating lesser sensitivity to precipitation changes.

The observed changes in the phase velocity of Rayleigh waves due to rainfall events stem from the fundamental principles of wave propagation in porous media. As the vadose zone becomes saturated, various seismic properties of the subsurface undergo substantial alterations.

A direct outcome of the water saturation is an increase in the soil's bulk modulus, attributable to water's near incompressibility. This results in an elevated compressional wave velocity (V_p). However, Rayleigh waves exhibit a stronger sensitivity to shear wave velocity V_s as opposed to V_p. This sensitivity has been empirically supported by multiple studies. Xia et al. (1999) showed that for the fundamental mode of high-frequency Rayleigh waves in a layered model, V_s is the dominant property affecting the Rayleigh wave's behavior. They reached this conclusion by comparing dispersion curves of models with 25 percent changes in each model parameter, namely V_s, V_p, density, and thickness. This finding was later extended to the higher modes by Xia et al. (2003). These studies underline the important role of V_s, which is primarily influenced by shear strength, in determining the changes in Rayleigh wave velocity.

The area under investigation predominantly features clayish soil, as documented in a USGS technical report (Pampeyan, 1993). The shear strength of this type of soil is governed by frictional resistance and particle interlocking, as well as interparticle forces (Stark et al., 2005). One crucial factor influencing shear strength, and thereby V_s, is the elevation in pore pressure induced by rainfall events. Excess pore pressure is particularly influential in clayey soils, leading to phenomena like hydroplaning, which substantially reduces internal friction (Mohrig et al., 1998; Anderson & Sitar, 1995). This increased pressure also reduces effective stress in the subsurface and can lead to the formation or widening of existing fractures, increasing the soil's porosity (Anderson & Sitar, 1995; Iverson, 1997). These alterations have direct implications on the shear strength of the soil, consequently influencing its V_s. Previous hydrogeophysical investigations utilizing both conventional broadband seismic and DAS technologies have reported consistent observations, notably a decrease in $\Delta v/v$ that correlates with elevated water table levels or seasonal rainfall patterns (Clements & Denolle, 2018; Lecocq et al., 2017; Rodríguez Tribaldos & Ajo-Franklin, 2021; Mao et al., 2022; Shen, 2022; Yang & Shragge, 2023). Additionally, the saturation process also modifies the subsurface's density. As water, possessing a greater density than air, fills the pore spaces, the bulk density of the soil or rock medium inherently rises. This augmentation in density typically results in a decrement in V_s (Knight & Nolen-Hoeksema, 1990).

6.2 Group-velocity tomography

In Figure 10, I presented the group velocity profiles derived from vehicles over two dry weeks. To discern the impact of rainfall on the group velocity along the fiber, we generated additional group-velocity profiles. These are based on averages of virtual shot gathers during a rainy two-week period in January for the frequencies of 6, 7, and 8 Hz. Figure 14 contrasts the profiles from dry and wet periods.

Two primarily non-built-up stretches, spanning 430 to 480 m and 650 to 670 m, exhibit a marked reduction in group velocity. In contrast, the constructed region near the 530-meter point manifests a subtler decrease. The substantial reduction in group velocity in less developed areas during rainfall can be ascribed to their enhanced perme-

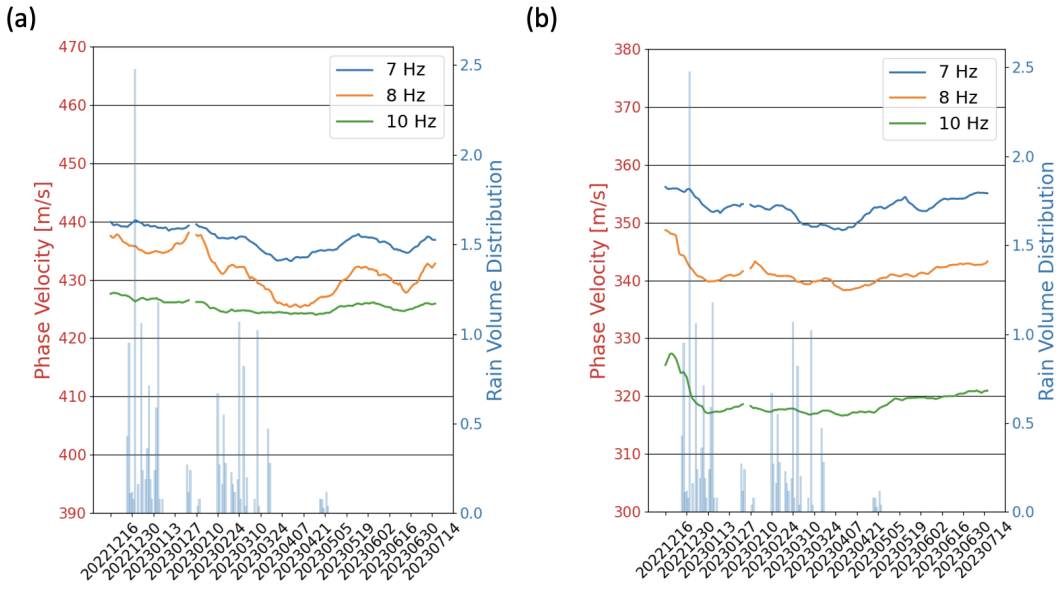

Figure 13. Phase velocity variation corresponding to different volumes of rainfall for two distinct fiber optic sections. (a) The section under the paved road, ranging from 490 m to 590 m; (b) The section under the grass, extending from 610 m to 710 m. The figure illustrates the influence of rainfall on the propagation characteristics in these distinct settings.

ability. This allows for more extensive water infiltration, leading to significant changes in subsurface characteristics.

In Figure 15, we show the temporal fluctuations of group velocity at the 430 m point within the lawn area1 for frequencies of 6 Hz and 7 Hz. These variations are plotted against the daily volume of rainfall within the same time span as depicted in Figure 13. The trend we observe aligns with the changes seen in phase velocity - a distinct reduction during the wetter months. Notably, towards the end of January, in the presence of reduced rainfall, a modest uptick in group velocity is evident. However, this resurgence is brief, as the group velocity diminishes once more with the commencement of rain in the wetter conditions of February and March. From April onward, during the drier months, we notice a steady recovery in the group velocity.

6.3 Seismic attenuation analyses

This subsection investigates the rain-induced property changes from an amplitude perspective. To investigate the influence of rainfall on seismic attenuation across the DAS array, we derived a Q^{-1} profile from recordings on both dry and wet days. In Figure 16, the blue curve represents the Q^{-1} profile deduced from dry day recordings, while the orange curve corresponds to those from wet days. It's noteworthy that heightened attenuation levels are evident in lesser-developed regions, particularly between the stretches of 430 - 500 meters and 650 - 750 meters.

Figure 17 exhibits the temporal Q^{-1} variations plotted against the daily rainfall volume at the 465 and 675-meter marks in the two lawn areas. This observation period aligns with the timeframes depicted in Figures 13 and 15. During rainfall events, there is a substantial increase in attenuation. Towards the end of January, when rainfall was less frequent, we notice a slight decrease in attenuation. However, during the rainfall events in February and March, the attenuation increases again. From April onward, we observe

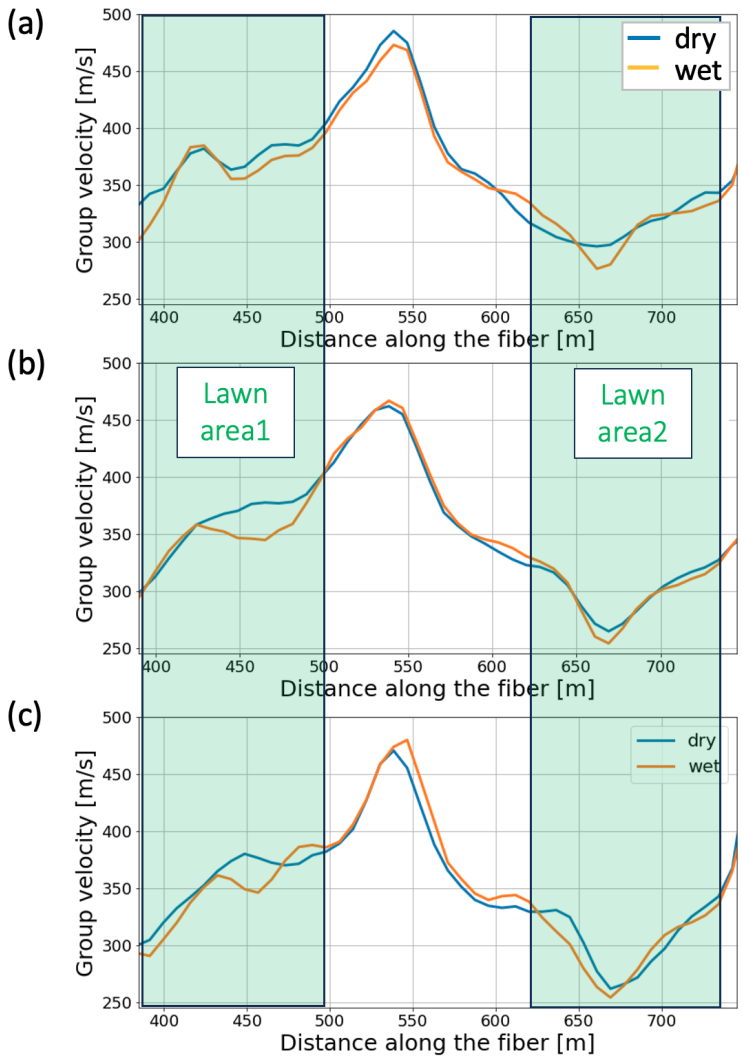

Figure 14. The group-velocity profile along the fiber. The blue curves in (a), (b), and (c) represent the profiles derived from averaging the virtual shot gathers over a dry two-week period in December for frequencies of 6, 7, and 8 Hz, respectively. The orange curves illustrate the profiles obtained by averaging virtual shot gathers over a wet two-week period in January for the same frequencies. These curves show a notable drop in group velocity at two relatively non-built-up areas, while the drop in the built-up region is less pronounced, indicating the influence of rainfall on group velocity along the fiber.

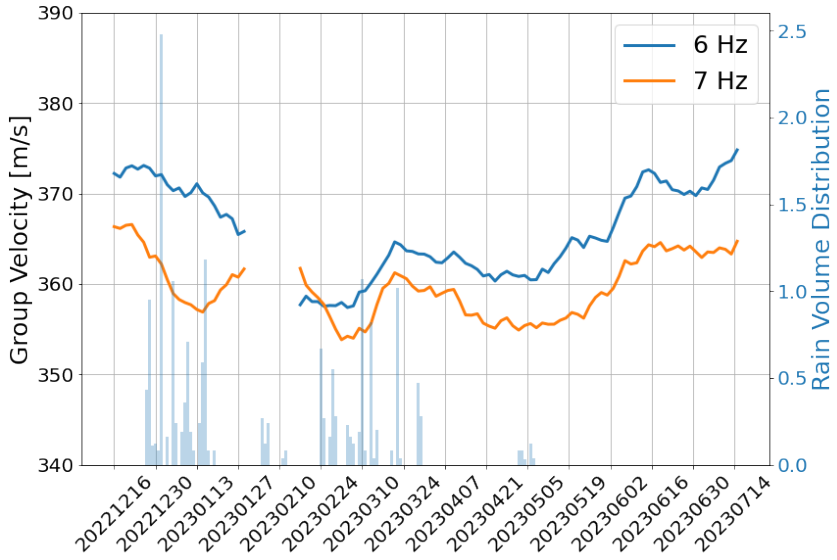

Figure 15. This figure displays the temporal variations in group velocity at the 430m mark within the lawn area1, as highlighted in Figure 14. The observed trend, characterized by a significant reduction in group velocity during the wetter months, shows a subtle resurgence in group velocity towards the end of January with reduced rainfall. The trend aligns with the variations observed in phase velocity, followed by recovery in group velocity during subsequent drier periods.

that attenuation gradually decreases during dry periods. This suggests that seismic waves are more strongly scattered and absorbed due to increased water content. One plausible explanation for this heightened attenuation during wet conditions is the increased pore pressure induced by rainfall. According to A. I. Best and McCann (1995); A. Best et al. (1994), the compliant and microporous nature of clay minerals in the soil allows for the phenomenon of squirt flow, which becomes more active with higher pore-fluid pressure. Squirt flow, involving rapid movement of fluids between tiny pores, effectively attenuates seismic waves as they pass through the medium. Therefore, the increased attenuation levels during rainfall events provide a sensitive measure of changes in soil saturation and pore pressure.

7 Conclusions

In this study, we introduce an innovative near-surface monitoring approach that uses vehicles as non-dedicated seismic sources. Our method enhances the traditional ambient noise interferometry by improving high-frequency sensitivity, boosting computational efficiency, and offering superior spatiotemporal resolution in subsurface monitoring. We have demonstrated the efficacy of our technique in monitoring rainfall-induced soil seismic property changes along a roadside DAS array at Stanford, achieving a level of spatiotemporal resolution previously impractical with traditional active source surveys and ambient noise interferometry. Our observations reveal significant alterations in phase and group velocity during rainfall events, as well as increases in seismic attenuation, particularly in non-built-up areas. These findings can potentially enhance urban water resource monitoring, including the early detection of water leakages.

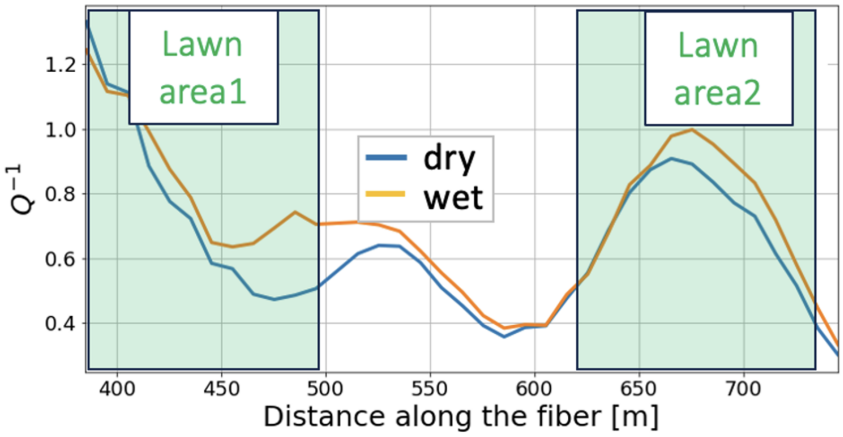

Figure 16. Q^{-1} profiles for dry and wet days. Higher attenuation due to the rain can be observed for 10 Hz.

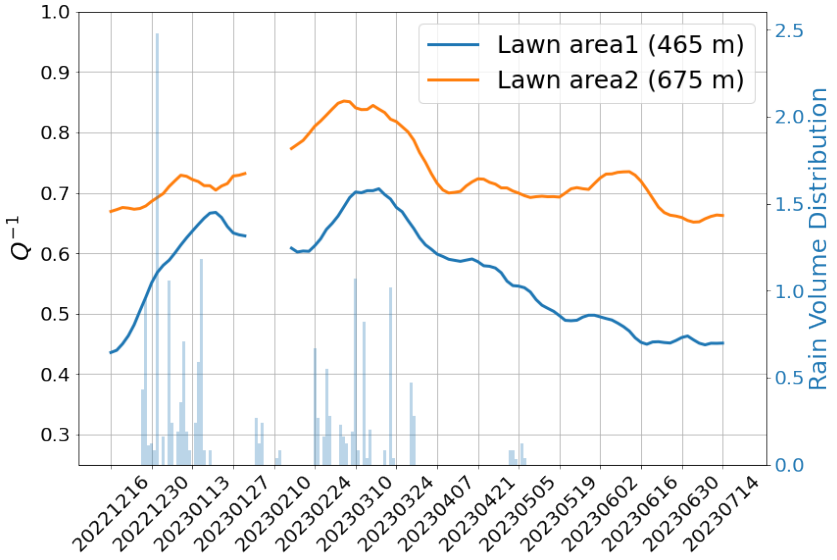

Figure 17. Temporal variations of the Q^{-1} parameter (estimated at 10 Hz) in correlation with the estimated daily rainfall volume at fiber ranges centered at 465 m and 675 m within the two lawn areas, over a timeframe consistent with Figures 13 and 15. A pronounced increase in attenuation is evident during rainfall events, whereas towards the end of January, a slight decrease in attenuation is observed due to reduced rainfall. This attenuation pattern then gradually reduces in drier periods following.

Data and Software Availability Statement

The data supporting the conclusions of this study are derived from continuous DAS recordings captured by the Stanford DAS-2 array. Due to the extensive size of the dataset, we selected ten days' recordings from December 15th to December 24th, 2022, during dry conditions. This data is publicly available at https://premonition.stanford.edu/syyuan/stanford-das-2-data-for-near-surface-characterization.

Separately, recordings from wet days in February 2023 have been published in line with the Global DAS Month initiative (NORSAR, 2023). This data set can be retrieved via the Globus platform, targeting the PubDAS endpoint (Spica et al., 2023). Navigate to the DAS-Month-02.2023/Stanford-SandHill/ directory for the DAS recordings. Direct access to the PubDAS Globus endpoint at the University of Michigan is facilitated through the following link: https://tinyurl.com/PubDAS.

The software for the proposed precision interferometry method introduced in the paper is publicly available in `https://github.com/syyuan93/das_veh`.

Acknowledgments

The interrogator unit was loaned to us by OptaSense Inc. We thank Martin Karrenbach, Victor Yartsev, and Lisa LaFlame from Optasense, as well as the Stanford ITS fiber team, and in particular Erich Snow, for crucial help with the Stanford DAS-2 experiment. We also thank the Stanford School of Earth IT team for hosting the interrogator in the Scholl computer room. We appreciate the insightful discussions with Qing Ji, Shujuan Mao, and Milad Bader. The Continuous Wavelet Transform (CWT) travel-time picking code is provided by Qing Ji. We thank Bin Luo for the ambient noise interferometry code.

References

Aki, K., & Richards, P. (2002). *Quantitative seismology* (2nd ed.). Sausalito, CA: Univ. Sci. Books.

Anderson, S. A., & Sitar, N. (1995). Analysis of rainfall-induced debris flows. *Journal of Geotechnical Engineering*, *121*(7), 544-552. Retrieved from `https://ascelibrary.org/doi/abs/10.1061/%28ASCE%290733-9410%281995%29121%3A7%28544%29` doi: 10.1061/(ASCE)0733-9410(1995)121:7(544)

Best, A., McCann, C., & Sothcott, J. (1994). The relationships between the velocities, attenuations and petrophysical properties of reservoir sedimentary rocks1. *Geophysical Prospecting*, *42*(2), 151-178. Retrieved from `https://onlinelibrary.wiley.com/doi/abs/10.1111/j.1365-2478.1994.tb00204.x` doi: https://doi.org/10.1111/j.1365-2478.1994.tb00204.x

Best, A. I., & McCann, C. (1995). Seismic attenuation and pore-fluid viscosity in clay-rich reservoir sandstones. *GEOPHYSICS*, *60*(5), 1386–1397.

Biondi, B. L., Yuan, S., Martin, E. R., Huot, F., & Clapp, R. G. (2021). Using telecommunication fiber infrastructure for earthquake monitoring and near-surface characterization. In *Distributed acoustic sensing in geophysics* (p. 131-148). American Geophysical Union (AGU). Retrieved from `https://agupubs.onlinelibrary.wiley.com/doi/abs/10.1002/9781119521808.ch10` doi: https://doi.org/10.1002/9781119521808.ch10

Chang, J. P. (2018). Imaging with ambient seismic noise: Beyond surface-wave microseisms. *ProQuest Dissertations and Theses*. Retrieved from `https://www.proquest.com/dissertations-theses/imaging-with-ambient-seismic-noise-beyond-surface/docview/2436917586/se-2` (Copyright - Database copyright ProQuest LLC; ProQuest does not claim copyright in the individual underlying works; Last updated - 2023-06-21)

Clements, T., & Denolle, M. A. (2018). Tracking groundwater levels using the

ambient seismic field. *Geophysical Research Letters*, *45*(13), 6459-6465. Retrieved from https://agupubs.onlinelibrary.wiley.com/doi/abs/10.1029/2018GL077706 doi: https://doi.org/10.1029/2018GL077706

de Ridder, S., & Dellinger, J. (2011). Ambient seismic noise eikonal tomography for near-surface imaging at valhall. *The Leading Edge*, *30*(5), 506-512. Retrieved from https://doi.org/10.1190/1.3589108 doi: 10.1190/1.3589108

Dou, S., Lindsey, N., Wagner, A. M., Daley, T. M., Freifeld, B., Robertson, M., ... Ajo-Franklin, J. B. (2017). Distributed acoustic sensing for seismic monitoring of the near surface: A traffic-noise interferometry case study. *Scientific Reports*, *7*. Retrieved from https://www.nature.com/articles/s41598-017-11986-4

Fang, G., Li, Y. E., Zhao, Y., & Martin, E. R. (2020). Urban near-surface seismic monitoring using distributed acoustic sensing. *Geophysical Research Letters*, *47*(6), e2019GL086115. Retrieved from https://agupubs.onlinelibrary.wiley.com/doi/abs/10.1029/2019GL086115 (e2019GL086115 10.1029/2019GL086115) doi: https://doi.org/10.1029/2019GL086115

Iverson, R. M. (1997). The physics of debris flows. *Reviews of Geophysics*, *35*(3), 245-296. Retrieved from https://agupubs.onlinelibrary.wiley.com/doi/abs/10.1029/97RG00426 doi: https://doi.org/10.1029/97RG00426

Knight, R., & Nolen-Hoeksema, R. (1990). A laboratory study of the dependence of elastic wave velocities on pore scale fluid distribution. *Geophysical Research Letters*, *17*(10), 1529–1532.

Lecocq, T., Longuevergne, L., Pedersen, H., et al. (2017). Monitoring ground water storage at mesoscale using seismic noise: 30 years of continuous observation and thermo-elastic and hydrological modeling. *Scientific Reports*, *7*, 14241. Retrieved from https://doi.org/10.1038/s41598-017-14468-9 doi: 10.1038/s41598-017-14468-9

Lin, F.-C., Li, D., Clayton, R. W., & Hollis, D. (2013). High-resolution 3d shallow crustal structure in long beach, california: Application of ambient noise tomography on a dense seismic array. *Geophysics*, *78*, Q45–Q56.

Lin, F.-C., Moschetti, M. P., & Ritzwoller, M. H. (2008, 04). Surface wave tomography of the western United States from ambient seismic noise: Rayleigh and Love wave phase velocity maps. *Geophysical Journal International*, *173*(1), 281-298. Retrieved from https://doi.org/10.1111/j.1365-246X.2008.03720.x doi: 10.1111/j.1365-246X.2008.03720.x

Liu, J., Yuan, S., Dong, Y., Biondi, B., & Noh, H. Y. (2023). *Telecomtm: A fine-grained and ubiquitous traffic monitoring system using pre-existing telecommunication fiber-optic cables as sensors.*

Liu, J., Yuan, S., Luo, B., Biondi, B., & Noh, H. Y. (2023). Turning telecommunication fiber-optic cables into distributed acoustic sensors for vibration-based bridge health monitoring. *Structural Control and Health Monitoring*, *2023*. Retrieved from https://doi.org/10.1155/2023/3902306

Louie, J. N. (2001). Faster, better: Shear-wave velocity to 100 meters depth from refraction microtremor arrays. *Bulletin of the Seismological Society of America*, *91*(2), 347. doi: 10.1785/0120000098

Mao, S., Lecointre, A., van der Hilst, R., et al. (2022). Space-time monitoring of groundwater fluctuations with passive seismic interferometry. *Nature Communications*, *13*, 4643. Retrieved from https://doi.org/10.1038/s41467-022-32194-3 doi: 10.1038/s41467-022-32194-3

Martin, E., Biondi, B., Karrenbach, M., & Cole, S. (2017). Ambient noise interferometry from das array in underground telecommunications conduits. In *79th conference and exhibition, eage, extended abstracts.*

Martin, E. R., Castillo, C. M., Cole, S., Sawasdee, P. S., Yuan, S., Clapp, R., ... Biondi, B. L. (2017, 12). Seismic monitoring leveraging existing telecom infrastructure at the SDASA: Active, passive, and ambient-noise analysis. *The*

Leading Edge, *36*(12), 1025-1031. Retrieved from https://doi.org/10.1190/tle36121025.1 doi: 10.1190/tle36121025.1

Martin, E. R., Lindsey, N. J., Ajo-Franklin, J. B., & Biondi, B. L. (2021). Introduction to interferometry of fiber-optic strain measurements. In *Distributed acoustic sensing in geophysics* (p. 111-129). American Geophysical Union (AGU). Retrieved from https://agupubs.onlinelibrary.wiley.com/doi/abs/10.1002/9781119521808.ch9 doi: https://doi.org/10.1002/9781119521808.ch9

Masoudi, A., & Newson, T. P. (2016). Contributed review: Distributed optical fibre dynamic strain sensing. *Review of Scientific Instruments*, *87*(1), 011501. Retrieved from https://doi.org/10.1063/1.4939482 doi: 10.1063/1.4939482

Mohrig, D., Ellis, C., Parker, G., Whipple, K. X., & Hondzo, M. (1998, 03). Hydroplaning of subaqueous debris flows. *GSA Bulletin*, *110*(3), 387-394. Retrieved from https://doi.org/10.1130/0016-7606(1998)110<0387:HOSDF>2.3.CO;2 doi: 10.1130/0016-7606(1998)110⟨0387:HOSDF⟩2.3.CO;2

Nazarian, S., Stokoe, K. H., & Hudson, W. R. (1983). Use of spectral analysis of surface waves method for determination of moduli and thicknesses of pavement systems. *Transportation Research Record*, 38-45. Retrieved from https://api.semanticscholar.org/CorpusID:58935998

NORSAR. (2023). *Global das monitoring month - february 2023.* Retrieved from https://www.norsar.no/in-focus/global-das-monitoring-month-february-2023

Optasense, a Luna company. (2022). *Quantx das interrogator: Optasense.* Retrieved from https://www.optasense.com/technology/quantx/

Pampeyan, E. H. (1993). *Geologic map of the palo alto and part of the redwood point 7-1/2' quadrangles, san mateo and santa clara counties, california* (Technical Report). U.S. Department of the Interior, USGS.

Park, C., Miller, R., & Xia, J. (1999). Multi-channel analysis of surface waves. *Geophysics*, *64*(3), 800–808.

Posey, R. (2000). Rayleigh scattering based distributed sensing system for structural monitoring. In A. G. Mignani & H. C. Lefèvre (Eds.), *Fourteenth international conference on optical fiber sensors* (Vol. 4185, p. 41850E). SPIE. Retrieved from https://doi.org/10.1117/12.2302157 doi: 10.1117/12.2302157

Rodríguez Tribaldos, V., & Ajo-Franklin, J. (2021, 03). Aquifer monitoring using ambient seismic noise recorded with distributed acoustic sensing (das) deployed on dark fiber. *Journal of Geophysical Research: Solid Earth*, *126*. doi: 10.1029/2020JB021004

Shapiro, N. M., & Campillo, M. (2004). Emergence of broadband rayleigh waves from correlations of the ambient seismic noise. *Geophysical Research Letters*, *31*(7). Retrieved from https://agupubs.onlinelibrary.wiley.com/doi/abs/10.1029/2004GL019491 doi: https://doi.org/10.1029/2004GL019491

Shapiro, N. M., Campillo, M., Stehly, L., & Ritzwoller, M. H. (2005). High-resolution surface-wave tomography from ambient seismic noise. *Science*, *307*(5715), 1615-1618. Retrieved from https://www.science.org/doi/abs/10.1126/science.1108339 doi: 10.1126/science.1108339

Shen, Z. (2022). *Probing water below the surface: Insights from seismic interferometry with conventional and das array* (Doctoral dissertation, California Institute of Technology). doi: 10.7907/5vtn-1c34

Spica, Z. J., Ajo-Franklin, J., Beroza, G. C., Biondi, B., Cheng, F., Gaite, B., ... Zhu, T. (2023, 01). Pubdas: A public distributed acoustic sensing datasets repository for geosciences. *Seismological Research Letters*.

Stark, T. D., Choi, H., & McCone, S. (2005). Drained shear strength parameters for analysis of landslides. *Journal of Geotechnical and Geoenvironmental Engineering*, *131*(5), 575–588.

Stokoe, K. H. I., Hwang, S., & Joh, S.-H. (2017). Spectral-analysis-of-surface-waves (sasw) testing to evaluate vs profiles at geotechnical and geological sites. In

16th world conference on earthquake engineering.

Wapenaar, K., Draganov, D., Snieder, R., Campman, X., & Verdel, A. (2010). Tutorial on seismic interferometry: Part 1 — basic principles and applications. *GEOPHYSICS*, *75*(5), 75A195-75A209. Retrieved from https://doi.org/10.1190/1.3457445 doi: 10.1190/1.3457445

Xia, J., Miller, R., & Park, C. (1999). Estimation of near-surface shear-wave velocity by inversion of rayleigh waves. *Geophysics*, *64*(3), 691–700.

Xia, J., Miller, R., Park, C., & Tian, G. (2003). Inversion of high frequency surface waves with fundamental and higher modes. *Journal of Applied Geophysics*, *52*(1), 45–57.

Yang, J., & Shragge, J. (2023, 04). Long-term ambient seismic interferometry for constraining seasonal subsurface velocity variations in urban settings: a distributed acoustic sensing (DAS) case study. *Geophysical Journal International*, *234*(3), 1973-1984. Retrieved from https://doi.org/10.1093/gji/ggad181 doi: 10.1093/gji/ggad181

Yuan, S., Lellouch, A., Clapp, R. G., & Biondi, B. (2020, 09). Near-surface characterization using a roadside distributed acoustic sensing array. *The Leading Edge*, *39*(9), 646-653. Retrieved from https://doi.org/10.1190/tle39090646.1 doi: 10.1190/tle39090646.1

Yuan, S., Liu, J., Young Noh, H., & Biondi, B. (2021). Urban system monitoring using combined vehicle onboard sensing and roadside distributed acoustic sensing. In *First international meeting for applied geoscience & energy* (pp. 3235–3239).

Zhao, Y., Nilot, E. A., Li, B., Fang, G., Luo, W., & Li, Y. E. (2023). Seismic attenuation extraction from traffic signals recorded by a single seismic station. *Geophysical Research Letters*, *50*(3), e2022GL100548. Retrieved from https://agupubs.onlinelibrary.wiley.com/doi/abs/10.1029/2022GL100548 (e2022GL100548 2022GL100548) doi: https://doi.org/10.1029/2022GL100548